Monthly Notices
of the
ROYAL ASTRONOMICAL SOCIETY

MNRAS **438,** 2395–2405 (2014)
Advance Access publication 2014 January 10

doi:10.1093/mnras/stt2356

A search for methane in the atmosphere of GJ 1214b via GTC narrow-band transmission spectrophotometry⋆

P. A. Wilson,[1]† K. D. Colón,[2,3] D. K. Sing,[1] G. E. Ballester,[4] J.-M. Désert,[5] D. Ehrenreich,[6] E. B. Ford,[3] J. J. Fortney,[7] A. Lecavelier des Etangs,[6] M. López-Morales,[8] C. V. Morley,[7] A. R. Pettitt,[1] F. Pont[1] and A. Vidal-Madjar[9]

[1]*Astrophysics Group, School of Physics, University of Exeter, Stocker Road, Exeter EX4 4QL, UK*
[2]*Department of Geology and Geophysics, University of Hawai'i at Manoa, Honolulu, HI 96822, USA*
[3]*Department of Astronomy, University of Florida, Gainesville, FL 32611, USA*
[4]*Lunar and Planetary Laboratory, University of Arizona, Sonett Space Sciences Building, Tucson, AZ 85721-0063, USA*
[5]*Caltech Division of Geological and Planetary Sciences, Pasadena, CA 91125, USA*
[6]*Observatoire astronomique de l'Université de Genève, 51 chemin des Maillettes, CH-1290 Sauverny, Switzerland*
[7]*Department of Astronomy and Astrophysics, University of California, Santa Cruz, CA 95064, USA*
[8]*Harvard–Smithsonian Center for Astrophysics, 60 Garden Street, Cambridge, MA 02138, USA*
[9]*Institut d'astrophysique de Paris, CNRS; Université Pierre et Marie Curie, 98 bis boulevard Arago, F-75014 Paris, France*

Accepted 2013 December 3. Received 2013 December 2; in original form 2013 May 31

ABSTRACT

We present narrow-band photometric measurements of the exoplanet GJ 1214b using the 10.4 m Gran Telescopio Canarias and the Optical System for Imaging and low Resolution Integrated Spectroscopy instrument. Using tuneable filters, we observed a total of five transits, three of which were observed at two wavelengths nearly simultaneously, producing a total of eight individual light curves, six of these probed the possible existence of a methane absorption feature in the 8770–8850 Å region at high resolution. We detect no increase in the planet-to-star radius ratio across the methane feature with a change in radius ratio of $\Delta\overline{R} = -0.0007 \pm 0.0017$ corresponding to a scaleheight (H) change of $-0.5 \pm 1.2H$ across the methane feature, assuming a hydrogen-dominated atmosphere. We find that a variety of water and cloudy atmospheric models fit the data well, but find that cloud-free models provide poor fits. These observations support a flat transmission spectrum resulting from the presence of a high-altitude haze or a water-rich atmosphere, in agreement with previous studies. In this study, the observations are pre-dominantly limited by the photometric quality and the limited number of data points (resulting from a long observing cadence), which make the determination of the systematic noise challenging. With tuneable filters capable of high-resolution measurements ($R \approx 600$–750) of narrow absorption features, the interpretation of our results are also limited by the absence of high-resolution methane models below 1 μm.

Key words: techniques: photometric – stars: individual: GJ 1214 – planetary systems.

1 INTRODUCTION

The discovery of close-in 'super-Earths', with masses between 1.5 and 10 $M_\oplus$, has opened an entirely new field of exoplanet research. While transiting super-Earths allow the radius and mass to be measured, the regime is prone to large degeneracies between their internal and atmospheric compositions and their masses (Rogers & Seager 2010). Characterizing the atmospheres may be the only way to help constrain the overall bulk composition of these hot planets. A large planet-to-star contrast is essential when measuring transmission or emission spectra, making transiting super-Earths orbiting M dwarf stars ideal for such studies.

The most studied super-Earth is GJ 1214b, discovered in the M Earth ground-based transit survey (Charbonneau et al. 2009). GJ 1214b is a 2.7 $R_\oplus$ planet orbiting a M4.5 dwarf star, and therefore has a large planet-to-star radius ratio despite the stellar radius only being 0.21 $R_\odot$. The result is a transit depth of nearly 1.5 per cent. The observed mass and radius of GJ 1214b are

⋆Based on observations made with the Gran Telescopio Canarias (GTC), installed at the Spanish Observatorio del Roque de los Muchachos of the Instituto de Astrofísica de Canarias, in the island of La Palma, and part of the large ESO program 182.C-2018 and the programs GTC2-10AFLO and GTC4-11AFLO.

† E-mail: paw@astro.ex.ac.uk

consistent with theoretical models indicative of a significant atmosphere (Miller-Ricci & Fortney 2010). Due to degeneracies in the models, it is predicted that GJ 1214b is either composed of a rocky/ice core surrounded by a hydrogen-rich atmosphere, a water/ice core with an atmosphere dominated by water vapour or a rocky core with a thin atmosphere formed by outgassing (Rogers & Seager 2010).

Recent studies have attempted to constrain GJ 1214b's atmosphere through transmission spectroscopy (Charbonneau et al. 2009; Bean, Miller-Ricci Kempton & Homeier 2010; Sada et al. 2010; Bean et al. 2011; Carter et al. 2011; Croll et al. 2011; Crossfield, Barman & Hansen 2011; Désert et al. 2011b; Kundurthy et al. 2011; Berta et al. 2012; de Mooij et al. 2012; Murgas et al. 2012; Colón & Gaidos 2013; Fraine et al. 2013; Narita et al. 2013a,b; Teske et al. 2013). In a majority of these studies, it has been found that GJ 1214b has a flat, featureless spectrum, with no evidence of any significant features either at optical (∼600–1000 nm) or near-infrared (1.1–1.7 μm) wavelengths. It is believed that the lack of significant features supports the presence of either a heavy, metal-rich atmosphere or optically thick clouds/hazes that produce a constant level of absorption across a large range of wavelengths. One exception is a study conducted by Croll et al. (2011). Specifically, they reported a significantly deeper transit depth at ∼2.15 μm, a wavelength where methane would be a viable source of opacity.

To help reconcile these studies, we present narrow-band photometry of five transits of GJ 1214b, three of them around a methane absorption feature commonly found at optical wavelengths in the atmospheres of the Jovian planets and Titan (Karkoschka 1994). The observations were acquired using the tuneable filter (TF) imaging mode on the Optical System for Imaging and low Resolution Integrated Spectroscopy (OSIRIS) instrument installed on the 10.4 m Gran Telescopio Canarias (GTC). TFs have several advantages over low-resolution spectroscopy; they provide accurate differential photometry whilst also allowing for relatively high-resolution measurements ($R \approx 600$–750), compared to low-resolution grisms. The relatively high resolution has the advantage of tuning the filters to avoid prominent telluric lines (see Hanuschik 2003 for a high-resolution sky emission atlas). Since no diffraction gratings are used, TFs can be much more efficient (Colón et al. 2010; Sing et al. 2011), especially for observing atomic absorption features that typically have a narrow spectral range. Combining this technique with the 10.4 m aperture of the GTC telescope makes it possible to study the atmospheres of planets orbiting fainter stars compared to the hot Jupiters HD 209458b and HD 189733b, which have bright host stars and large atmospheric scaleheights, making them two best studied cases thus far.

The methane feature that we focus on is the blue edge of the methane absorption band at 8900 Å and is predicted to cause additional absorption during transit at a level of ∼0.1 per cent, assuming a hydrogen-rich atmosphere (Berta et al. 2011). In Section 2, we describe our observations. In Sections 3 and 4, we describe our data reduction and analysis procedures. We present our results in Section 5, where we also discuss the implications of stellar activity, equilibrium cloud models and the possible presence of methane in the atmosphere of GJ 1214b. Finally, we conclude with a summary of our findings in Section 6.

2 OBSERVATIONS

Photometric observations of GJ 1214b were conducted using the GTC telescope on La Palma. For all observations, we used the TF imaging mode on OSIRIS (Cepa 1998; Cepa et al. 2000, 2003) to acquire photometry within a bandpass of 12 Å. The TF imager allows for custom bandpasses with a central wavelength between 651–934.5 nm and a full width at half-maximum (FWHM) of 12–20 Å to be specified.

Out of the five transits observed, three transits were observed in the 8770–8850 Å region by alternating between two narrow bandpasses, each with an FWHM of 12 Å, allowing us to perform near simultaneous photometry at two wavelengths. Observing one transit at two wavelengths simultaneously allows for a more accurate comparison between two wavelengths as systematic variations caused by varying weather conditions or stellar activity are likely to affect both light curves similarly. For the observations done at two wavelengths, we specifically chose our bandpasses so that one was located in the continuum, at a shorter wavelength of 8770 and 8784.5 Å compared to the other band located at 8835 and 8849.6 Å, within the methane absorption band. As described in Colón et al. (2010) and Sing et al. (2011), another property of the TF imaging mode is that the effective wavelength decreases radially outwards from the optical centre, so we attempted to position the target and a single 'primary' reference star (i.e. one most comparable in brightness to the target) at the same distance from the optical centre so as to observe both stars at the same wavelengths.[1] The other reference stars were thus observed at slightly different wavelengths than the target, due to their different distances from the optical centre.

All observations were performed with 1×1 binning and a fast pixel readout rate of 500 kHz, a gain of 1.46 e^-/ADU and a read noise of $\sim 8e^-$ as well as a single window located on one CCD chip. The size of the window varied for each observation, but was chosen to be large enough so as to contain the target and several reference stars of similar brightness. Data points with analogue-to-digital unit (ADU) counts larger than 45 000 were removed to ensure the measurements were taken in the linear regime of the CCD detector. The data presented in this paper originated from two separate observing programmes by PI. D. Sing (ESO programme 182.C-2018; see Sections 2.1 and 2.2) and PI. K. Colón (GTC2-10AFLO and GTC4-11AFLO; see Sections 2.3–2.5) and each had slightly different observing strategies. Further details regarding each specific transit observation are given in the following sections.

2.1 8100 Å transit, 2010 August 17

Observations of the 2010 August 17 transit were tuned to a target wavelength of 8100 Å, with the target 3.7 arcmin away from the optical centre. The observations began at 21:18 UT and ended at 23:29 UT, during which time the airmass ranged from 1.11 to 1.44. Due to variable seeing, ranging from 0.7 to 1.2 arcsec, the telescope was defocused to avoid saturation. Two reference stars were selected (more on the selection technique in Section 3). The observations were windowed using a 1160×760 pixel section on CCD1. 12 images containing counts greater than 45 000 ADUs were removed to ensure linearity. The exposure time was kept at 60 s throughout the sequence, with a corresponding ∼12 s of readout time.

2.2 8550 Å transit, 2010 June 2

Observations of the 2010 June 2 transit were tuned to a target wavelength of 8550 Å, with the target 1.3 arcmin from the optical centre.

[1] Due to technical issues, the positioning for some of the observations was not as expected, and the target and a single reference star were not always observed at the same exact wavelengths. See Section 4.3.

The observations began at 23:48 UT and ended at 03:04 UT, during which time the airmass ranged from 1.27 to 1.87. Due to a technical problem with the secondary mirror, re-focusing was not possible during the whole sequence. This caused an increase in the FWHM of the point spread function (PSF) of the stars from 0.9 to 1.9 arcsec, resulting in a notable decrease in the peak counts levels. Three reference stars were selected. The observations were performed using CCD1 and no windowing was done. One data point with counts greater than 45 000 ADUs was removed to ensure linearity (see Section 3). The exposure time was kept at 120 s throughout the sequence, with a corresponding ∼24.5 s of readout time for the full frame.

2.3 8770 and 8835 Å transit, 2010 August 28

Observations of the 2010 August 28 transit were tuned to the target wavelengths of 8770 and 8835 Å, with the target 3.2 arcmin from the optical centre. The observations were done by alternating between the two wavelengths in sets of two exposures at each wavelength. The seeing was variable throughout the observations, so the telescope was defocused and the exposure time was changed to avoid saturation. The observations were done in queue (service) mode. The exposure time started at 100 s and was later increased to 150 s and then to 200 s towards the end of the observations. The observations began at 22:00 UT and ended at 00:30 UT, during which time the airmass ranged from 1.26 to 2.32 and the FWHM varied between 1.0 and 2.6 arcsec. There are some small gaps in the data towards the beginning of the observations due to minor technical issues. Also, there is some vignetting in the last few images due to the low elevation of the telescope, so we exclude these from our analysis. Two reference stars were selected. Two data points with counts greater than 45 000 ADUs were removed to ensure linearity. The observations were windowed using a 850 × 4102 pixel section on CCD2 with a corresponding ∼22 s of readout time.

2.4 8770 and 8835 Å transit, 2011 June 10

Observations of the 2011 June 10 transit were tuned to the target wavelengths of 8770 and 8835 Å with the target 3.2 arcmin from the optical centre. The observations were done by alternating between the two wavelengths in sets of two exposures at each wavelength. The conditions were clear, and observations took place during bright time in visitor mode. Observations began at 23:40 UT and ended at 02:48 UT, during which time the airmass ranged from 1.09 to 1.19 and the FWHM varied between 1.3 and 2.2 arcsec. The observations started 25 min later than planned because one of the M1 mirror segments was found to be slightly misaligned (see Fig. 1). One segment of the mirror would not stack with the other segments. Attempts were made to correct this, although the problem persisted throughout the observations. As this problem had the same effect on all the stars (i.e. each star had an extended PSF; see Fig. 1), we have assumed that the photometry was not significantly affected by this problem since we chose a larger aperture that included the photons from the unstacked segment. Three reference stars were selected. The observations were windowed using a 850 × 3250 pixel section on CCD1. An exposure time of 100 s was used throughout the sequence, with a corresponding ∼19 s of readout time.

2.5 8784.5 and 8849.6 Å transit, 2010 July 21

Observations of the 2010 July 21 transit were tuned to the target wavelengths of 8784.5 and 8849.6 Å, with the target 2.9 arcmin from the optical centre. The observations were done by alternating between the two wavelengths in sets of two exposures at each wavelength. The conditions were clear and the observations took place during bright time in queue mode. The observations began at 00:26 UT and ended at 02:11 UT. The airmass ranged from 1.25 to 1.87. The actual seeing varied between 0.9 and 1.4 arcsec. A slight defocus was used in order to avoid saturation. Two reference stars were selected. The observations were windowed using a 849 × 3774 pixel section on CCD2. An exposure time of 120 s was used throughout the sequence with a corresponding ∼22 s of readout time.

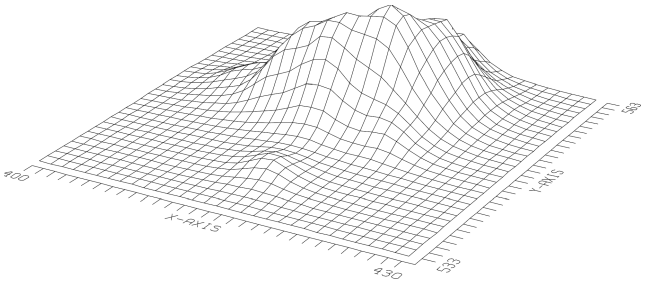

Figure 1. A surface plot of GJ 1214 showing an uneven PSF due to a misalignment of the M1 mirror during the 8770 and 8835 Å observations on 2011 June 10 (see Section 2.4). The small bump seen towards the front of the larger PSF is due to one of the hexagonal mirrors not being properly aligned. By choosing a larger photometry aperture, the effects caused by the distorted PSF were removed.

3 DATA REDUCTION

For all our data sets, we used standard IRAF[2] procedures for bias subtraction and flat-field correction. For the flat-field correction, we used dome flats that were taken after each observation and for each filter setting. For the observations done at the methane-probing wavelengths 8770 (two transits), 8784.5, 8835.0 (two transits) and 8849.6 Å were affected by the presence of sky lines. We therefore performed a sky subtraction of these images using the IRAF package TFRED.[3]

Aperture photometry was done using the APPHOT package in IRAF. To obtain the best-possible photometry, a large number of apertures and sky annuli were explored. The aperture and sky annulus combination which produced the least amount of scatter in the continuum (lowest χ^2 value by fitting a straight line to the continuum) was chosen. The number of reference stars varied depending on the size of the CCD readout window, the location of the sky lines as well as the observed scatter in the photometry of each reference star. To determine the optimal number of reference stars, all stars above 15 000 ADUs were initially chosen as potential reference stars. Each star which did not help reduce the overall scatter in the continuum, such as fainter stars affected by the sky emission rings (see Section 4.3), was removed.

The linearities of the CCD1 and CCD2 detectors were evaluated by measuring the average ADU counts of centrally windowed

[2] IRAF is distributed by the National Optical Astronomy Observatories, which are operated by the Association of Universities for Research in Astronomy, Inc., under cooperative agreement with the National Science Foundation.
[3] Written by D. H. Jones for the Taurus Tunable Filter, previously installed on the Anglo-Australian Telescope; http://www.aao.gov.au/local/www/jbh/ttf/adv_reduc.html.

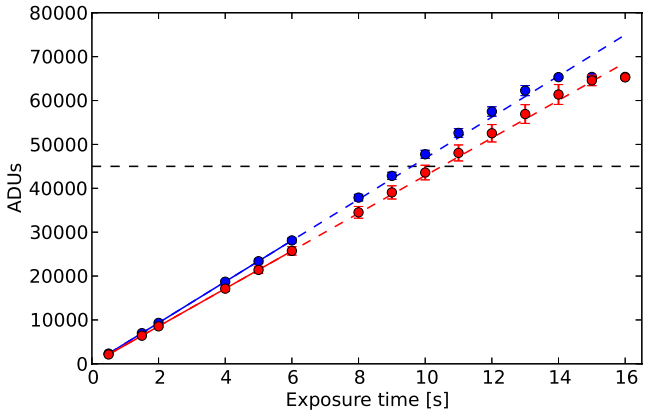

Figure 2. The OSIRIS CCD1 (red) and CCD2 (blue) 500 kHz exposure curves showing the linearity of the detector. The measurements connected by a solid line were used to fit the estimated linearity of the detector. Images which had the brighter reference star at more than 45 000 ADUs were removed in order to ensure that they used data sampled within the linear regime of the CCD.

flat-field images as a function of exposure time (see Fig. 2). Using the measured points known to be within the linear regime of the CCD (<25 000 ADUs), a linear extrapolation of ADUs as a function of exposure time was created. To ensure that the observations were not affected by non-linearity effects, the few images that contained a reference star with more than 45 000 ADUs were discarded, as counts above this level were shown to deviate from the linear extrapolation by more than 1σ on CCD2. The resulting light curves are shown in Figs 3 and 4.

4 ANALYSIS

4.1 Light-curve fits

The transit light curves were fitted using the analytical transit equations of Mandel & Agol (2002). The best-fitting light curve, together with the uncertainties associated with the fits, were determined by performing a Markov chain Monte Carlo algorithm (MCMC); see Gregory (2005) for the use of MCMC in uncertainty estimates, Collier Cameron et al. (2007) for the application to transit fitting and Pont et al. (2009) for our specific implementation. This gave us a posterior probability distribution which we used to define the uncertainties (see Section 4.4 and Fig. 5). For a discussion on how the short baselines affect the radius ratio uncertainties, we refer the reader to Appendix A. Individual light-curve fits were generated for each transit corresponding to different wavelengths. The initial starting parameters were from Bean et al. (2011); see below. We used 5 chains each consisting of 500 000 steps, trimming away the first 50 000 points with an ∼25 per cent of the proposed parameter steps being accepted.

The free parameters in the fit were the radius ratio, R_p/R_s and the sky-ring positions outlined in Section 4.3 and summarized in Table 1. The fixed parameters were the period $P = 1.580\,404\,81$ d, mid-transit time $T_0 = 245\,4966.525\,123$ $\mathrm{BJD_{TDB}}$ (see Table 1 for calculated ephemerides), impact parameter $b = 0.277\,29$ and the quadratic limb-darkening coefficients, u_1 and u_2, which varied depending on the wavelength of the observations. The stellar and orbital parameters were also kept fixed with $R_s = 0.21\,R_\odot$, the eccentricity $e = 0$ and the scaled semimajor axis $a/R_s = 14.9749$. We fix these values to allow for a more accurate comparison with Bean et al. (2010), Désert et al. (2011b), Croll et al. (2011) and Berta et al. (2012).

The limb-darkening coefficients used were calculated using the ATLAS stellar atmospheric models[4] following Sing (2010) and are listed in Table 1. A quadratic limb-darkening law of the following form was used:

$$\frac{I(\mu)}{I(1)} = 1 - u_1(1-\mu) - u_2(1-\mu)^2, \quad (1)$$

where $I(1)$ is the intensity at the centre of the stellar disc, $\mu = \cos(\theta)$ is the angle between the line of sight and the emergent intensity while u_1 and u_2 are the limb-darkening coefficients.

4.2 The effects of Earth's atmosphere

In an attempt to assess the photometric variability caused by the Earth's atmosphere, we studied the ratio of the reference star fluxes as a function of time and looked for correlations such as detector position, airmass, FWHM and the position of the OH emission sky lines present in the data (see Fig. 6). In order to determine which correlations were significant, the Bayesian Information Criterion (BIC) was computed and the model with the lowest BIC was accepted. The position of the OH sky emission rings, which were only visible in the images observed around the methane feature, was the dominant systematic effect occurring when a sky ring drifted across either the target or the reference stars. The sky-position was found to behave linearly throughout the observing sequence and was modelled by a linear fit to the position of the sky rings. For the data with no sky lines present, a slope term was used to correct for the slope of the out-of-transit flux. The effects of airmass and FWHM were present, but not strong enough to warrant any detrending. In the case of the slight FWHM trends, they seemed to mainly influence the data under variable seeing conditions. The light curves with their associated correlations were all fitted simultaneously by performing an MCMC. A summary of the results can be seen in Table 1.

4.3 The presence of sky lines

When using the TFs on the OSIRIS instrument, the observed wavelength decreases radially outwards from the centre of the TF due to a difference in the optical path length that the light has to travel. This effectively causes most of the stars in the field to be observed at slightly different wavelengths. The functional form of this radial wavelength dependence can be described using the following equation:

$$\lambda(r) = \lambda_0 - 5.04 \times r^2 + a(\lambda) \times r^3, \quad (2)$$

where the chromatic colour term is expressed as $a(\lambda) = 6.1781 - 1.6024 \times 10^{-3} \times \lambda + 1.0215 \times 10^{-7} \times \lambda^2$, where λ_0 (Å) is the central wavelength at which the TF is tuned and r (arcmin) is the distance outwards from this centre. The effects of the radial wavelength dependence are easily seen in Fig. 6 where the prominent OH sky lines are visible. Ideally, each exposure is taken at the same wavelength throughout an observing sequence within a tolerance typically of 1–2 Å; however, this is not the case for these observations. At the methane-probing wavelengths 8770, 8784.5 and 8835.0 Å, a clear drift in wavelength is observed (see Fig. 7). This causes systematic effects in the observations when a significant portion of the sky ring crosses either the target star or the reference stars. A linear combination of sky-ring position of the

[4] http://kurucz.harvard.edu/grids.html

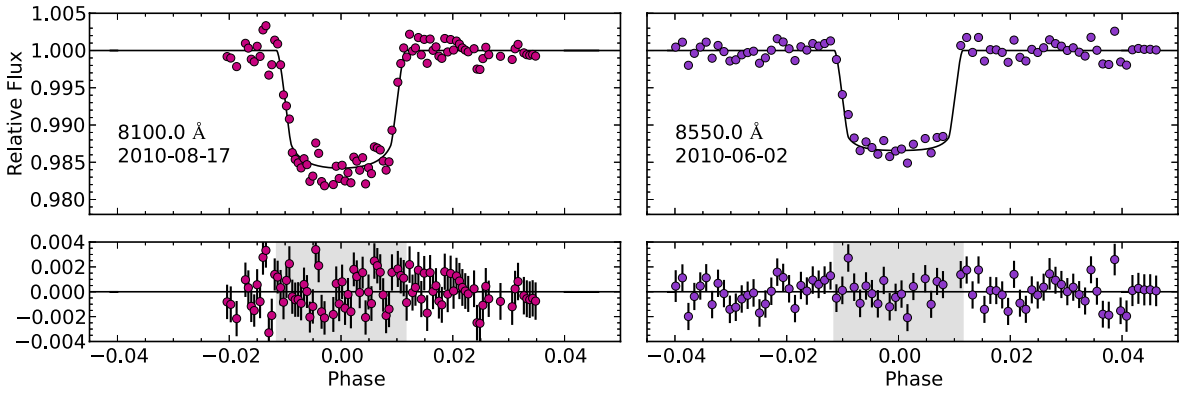

Figure 3. The GTC OSIRIS narrow-band light curves with the target wavelength tuned to 8100.0 (left) and 8550.0 Å (right). Below each light curve are the residuals from the best fit. The 8550.0 Å light curve has a considerable shallower transit depth compared to the other transits. This could be due, in part, to a below average number of star spots on the surface of GJ 1214 effectively creating a shallower transit depth.

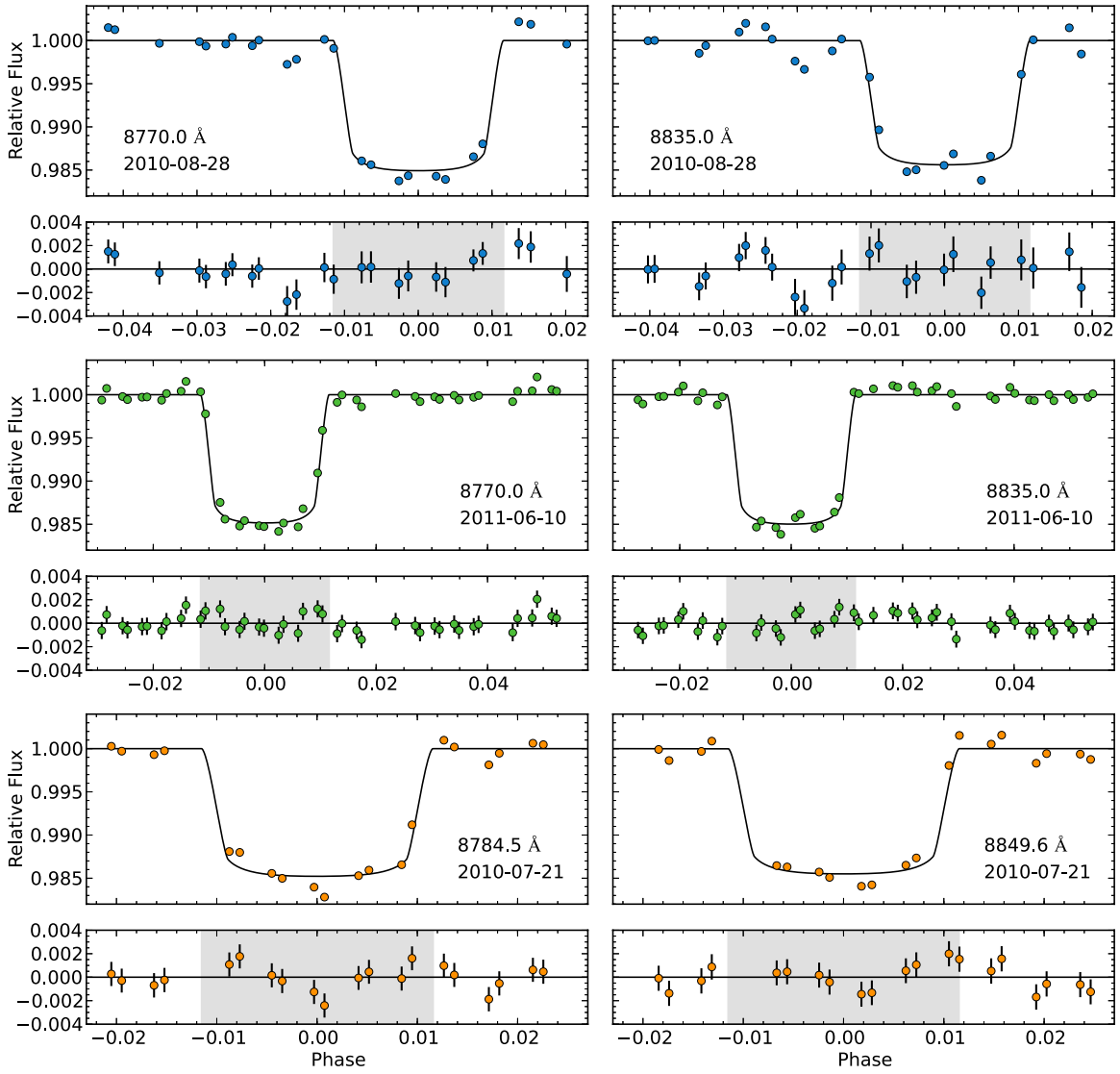

Figure 4. The GTC OSIRIS narrow-band light curves at the off-methane target wavelengths 8770 Å (two transits) and 8784.5 Å (on the left) and the methane-probing target wavelengths 8835.0 Å (two transits) and 8849.6 Å (on the right). Below each light curve are the residuals from the best fit.

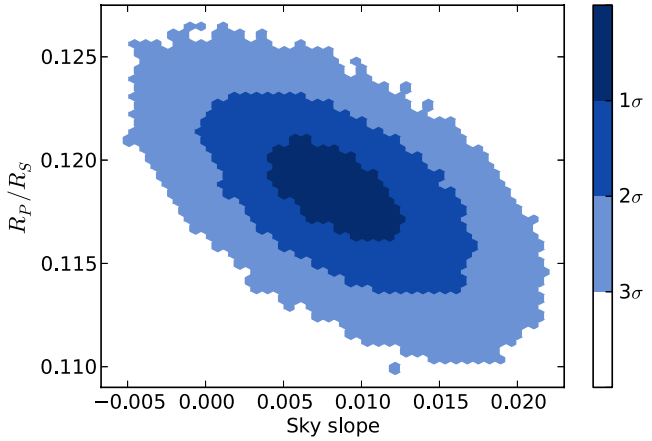

Figure 5. The posterior MCMC distribution showing the relationship between the radius ratio and the slope of the sky term for the 8770.0 Å observations on 2011 June 10. The different shadings represents the 1σ (dark-blue), 2σ (mid-blue) and 3σ (light-blue) confidence intervals.

form $A \times \text{sky} + B$ was multiplied by the light-curve fit, with sky being the sky-ring position and A and B being parameters set to vary freely in order to detrend this systematic effect. For the observations at 8100, 8550 and 8849.6 Å, there were no interfering sky lines present in the data.

4.4 Noise estimate

The resulting light curves shown in Figs 3 and 4 are affected by both white noise (noise uncorrelated with time, such as photon noise) as well as red noise (noise which correlates with time, such as airmass). In order to obtain realistic uncertainties, the red noise must be taken into account, since only using Poisson noise can underestimate the uncertainties. We estimated the level of white noise (σ_w) and red noise (σ_r) using techniques described in Pont, Zucker & Queloz (2006). The relationship between σ_w and σ_r is given by

$$\sigma_1^2 = \sigma_w^2 + \sigma_r^2, \tag{3}$$

where σ_1 is the standard deviation of the unbinned residuals, i.e. the difference between the individual normalized flux measurements and the best-fitting models of the transit light curves. In the absence of red noise, the standard deviation in the binned residuals is expressed as

$$\sigma_N = \frac{\sigma_1}{\sqrt{N}}\sqrt{\frac{M}{M-1}}, \tag{4}$$

where M is the number of bins each containing N points. However, since σ_N is in most cases larger than the above-calculated value

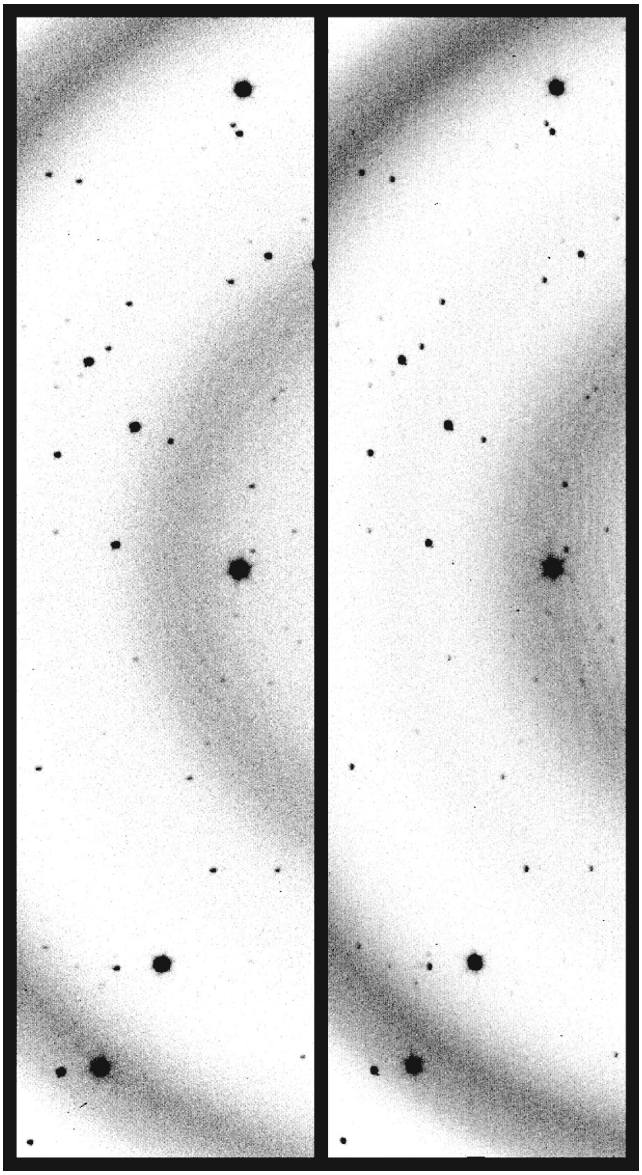

Figure 6. These two images exemplify the drift in OH sky emission observed during an observing sequence. The image on the left was taken at the beginning of the sequence, whilst the image on the right was taken towards the end of the sequence during the 8770.0 Å observations on 2011 June 10. For some of the observations, a linear correlation with sky-line position was found and used to detrend the systematic effects it was causing in the data.

Table 1. System parameters for GJ 1214b[a].

Wavelength	R_p/R_s	BJD_{TDB}	Date	u_1	u_2	Trends	σ_1	σ_r
8100.0 Å	0.120 38 ± 0.0013	245 5426.422 923	2010-08-17	0.1797	0.3200	None	0.001 41	0.000 20
8550.0 Å	0.110 42 ± 0.0014	245 5350.563 492	2010-06-02	0.0552	0.3029	None	0.001 07	0.000 28
8770.0 Å	0.118 43 ± 0.0025	245 5437.487 593	2010-08-28	0.0552	0.3243	Sky-ring position	0.001 16	0.000 42
8770.0 Å	0.117 54 ± 0.0016	245 5723.539 027	2011-06-10	0.0552	0.3243	Sky-ring position	0.000 73	0.000 34
8784.5 Å	0.117 24 ± 0.0020	245 5399.556 041	2010-07-21	0.0556	0.3266	Sky-ring position	0.001 02	0.000 43
8835.0 Å	0.115 56 ± 0.0032	245 5437.487 593	2010-08-28	0.0577	0.3357	Sky-ring position	0.001 40	0.000 48
8835.0 Å	0.117 91 ± 0.0016	245 5723.539 027	2011-06-10	0.0577	0.3357	Sky-ring position	0.000 71	0.000 37
8849.6 Å	0.115 95 ± 0.0024	245 5399.556 041	2010-07-21	0.0584	0.3387	None	0.001 07	0.000 49

[a] Ephemeris from Bean et al. (2011) with $P = 1.580\,404\,81 \pm 1.2\text{E}-7$ d and $T_c = 245\,4966.525\,123 \pm 0.000\,032$ BJD_{TDB}.

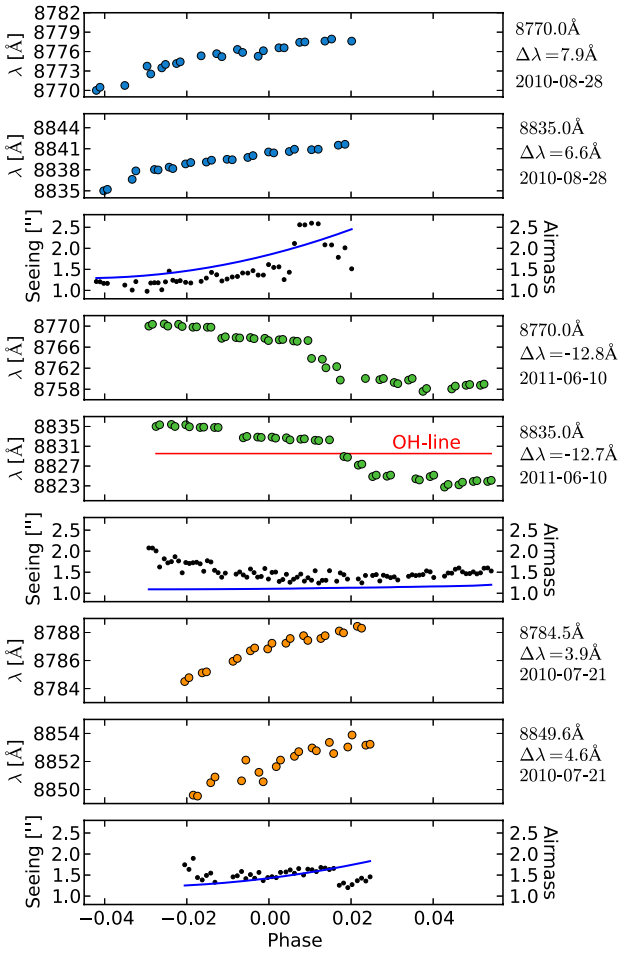

Figure 7. The panels show the drift in wavelengths during each observation together with the changes in seeing and airmass. The seeing is indicated by black points (seeing scale on the left) whilst airmass is represented by a blue solid line in the same panel (aimrass scale on the right). The red line shown in the fifth panel from the top shows the location of the OH sky-line doublet near 8829.5 Å. The drift in wavelength was calculated using equation (2).

(equation 4) due to the presence of red noise, the effects of red noise on the radius ratio had to be taken into account by using a re-weighting factor. The contribution by red noise was estimated by choosing N to be equal to the number of points in the transit, which varied in accordance with the cadence of the observations and can be written as

$$\sigma_{\rm r} = \sqrt{\sigma_N^2 - \frac{\sigma_{\rm w}^2}{N}}. \quad (5)$$

The red noise was then used to recompute the error bars, taking systematic noise into account by using a re-weighting factor, β, expressed as

$$\beta = \frac{\sigma_{\rm r}}{\sigma_{\rm w}}\sqrt{N}. \quad (6)$$

The individual parameters used in the light-curve fitting together with the estimated white and red noise are summarized in Table 1.

5 RESULTS AND DISCUSSION

The resulting light curves with their corresponding best-fitting models for each transit observation are shown in Figs 3 and 4. The measured radius ratios are compared to atmospheric models by Morley et al. (2013) and are shown in Figs 8 and 9.

5.1 Variability due to stellar activity

GJ 1214, an active M4.5-type star, has been shown to exhibit an ∼2 per cent peak-to-peak stellar flux variability in the wavelength range 715–1000 nm and a long rotation period of the order of 53 d (Berta et al. 2011) based on three years of data from MEarth (Nutzman & Charbonneau 2008). This is equivalent to a difference in radius ratio of $\Delta(R_{\rm p}/R_{\rm s}) \sim 0.001$ (using equation 7 from Désert et al. 2011a). Compared to the equilibrium cloud model atmosphere, which includes methane, detailed in Section 5.4, we would expect an increase in the radius ratio of the broad methane absorption band at 8800–9000 Å to be $R_{\rm p}/R_{\rm s} \sim 0.002$ at the resolution of our measurements. As such, it is necessary to consider the impact of stellar variability and star spots.

The stellar activity can affect the transit depth by means of unocculted star spots, which increase the transit depth, or by the presence of occulted star spots, which lead to an underestimation of the transit depth. As the star spot coverage changes due to the evolution of the spots and stellar rotation, it is possible that small differences in the transit depths are measured at different epochs. To limit the effects of stellar activity, it is essential that the different wavelength observations are done at, or close to, the same time. In this study, the light curves that probed the methane feature were acquired over three transits by alternating the TFs between two wavelengths. This gave a total of six individual transits around the methane feature (see Fig. 4), two at 8770 Å and one at 8784.5 Å (off-methane) and two at 8835 Å and 8849.6 Å (on-methane).

The transit light curve at 8550 Å taken on 2010 June 2 shows a considerably shallower transit depth inconsistent at the ∼3σ significance level with previously measured radius ratios by Bean et al. (2011). Although the cause of this is unknown, it is possible that the shallower light curve is partly the result of a below average number of star spots on the surface of GJ 1214, causing a shallower transit depth to be observed. No evidence for the presence of an occulted star spot is present in the data. Carter et al. (2011) also observed a shallower transit of GJ 1214b three nights later, during the morning of the 2010 June 6 (see Fig. 10, near BJD-245 5260 + 90). Considering that the estimated rotation speed of GJ 1214b is of the order of 53 d, it is likely that both observations were affected by a lower number of star spots than usual.

5.2 The impact of the observed wavelength drifts

The change in sky-line position during the course of the observations is indicative of a change in wavelength. By measuring the position of the sky lines in the images, the corresponding drift in wavelength was estimated following equation (2) with the drifts shown in Fig. 7. The most significant wavelength drift is seen in the 2011 June 10 observations where a wavelength change of ∼13 Å was observed. No detectable sky lines were observed during the 2010 August 17 and 2010 June 2 observations.

Although every attempt was made to tune the filter to a wavelength absent of strong sky lines, it is likely that the sky lines still affect the data despite the sky background having been subtracted. In particular, the OH emission-line doublet at 8829.514 and 8829.525 Å (Rousselot et al. 2000) has likely interacted with the 8835 Å observations conducted on 2011 June 10. The 8770 Å observations, conducted the same night, are not affected by a similar shift in wavelength which suggests that the OH emission line

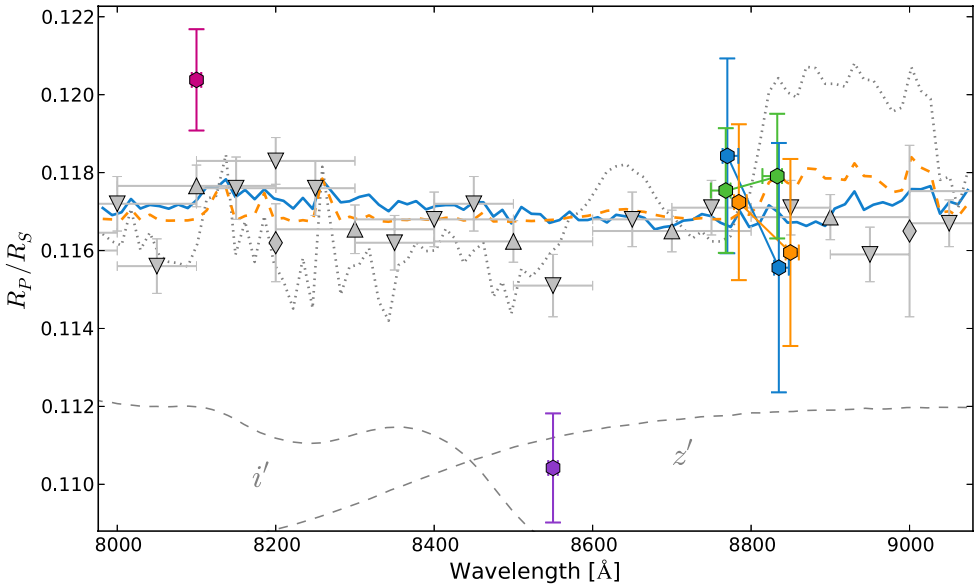

Figure 8. The combined transmission spectrum of GJ 1214b with data from Bean et al. (2010, grey upward triangles) and Bean et al. (2011, grey downward triangles) using the FORS instrument on the VLT (200 Å bandpass), de Mooij et al. (2012) using the *I* filter with the WFC on the Isaac Newton Telescope and z filter with the GROND instrument on the 2.2 m MPI/ESO telescope (grey diamond) and this study (multicoloured hexagonal markers, 12 Å bandpass). The horizontal error bars represent the width of the photometric band. The transmission spectra are from Morley et al. (2013) and have been binned into 12 Å bins for clarity. The observations are shown alongside a 100 per cent water atmosphere model (solid blue line), a best-fitting cloud-free 50 × solar composition atmosphere model with an efficient heat distribution (grey dotted line) and a worst-fitting cloudy (KCl and ZnS) 50 × solar composition atmosphere model with a low sedimentation efficiency of $f_{\rm sed} = 0.1$ and an efficient heat distribution (orange dashed line). A close-up of the methane-probing region is shown in Fig. 9.

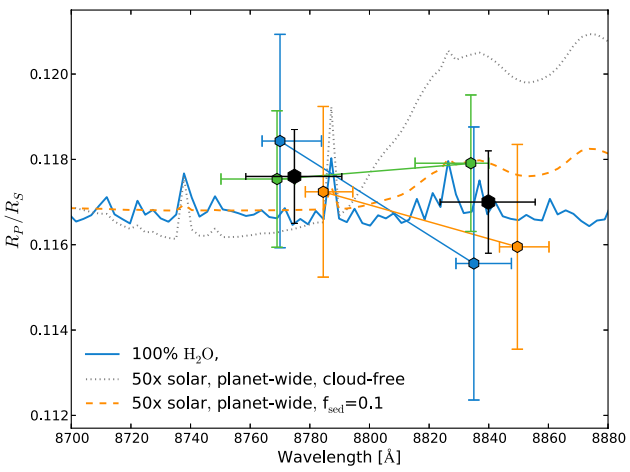

Figure 9. The weighted average of the on-methane and off-methane radius ratios (black points) compared to unbinned model spectra of a 100 per cent water atmosphere model (blue solid line), a best-fitting cloud-free 50 × solar composition atmosphere model with an efficient heat distribution (grey dotted line) and a cloudy (KCl and ZnS) 50 × solar composition atmosphere model with a low sedimentation efficiency of $f_{\rm sed} = 0.1$ and an efficient heat distribution (orange dashed line). The coloured points represent the radius ratios from the individual transits. For a larger overview of the transmission spectrum, see Fig. 8.

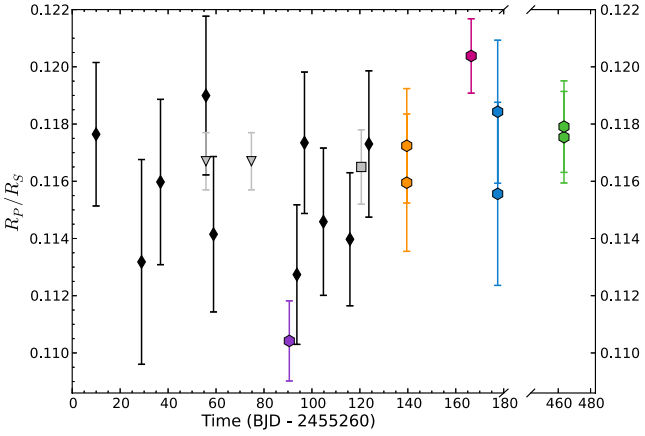

Figure 10. Shown are the radius ratios as a function of time (BJD), spanning a time period from 2009 May 29 until 2011 June 10. The black diamonds are measurements by Carter et al. (2011) in the Sloan z' band using the 1.2 m FLWO telescope. The grey triangles represent the VLT measurements by Berta et al. (2011) in the z' band. The grey squares represents the de Mooij et al. (2012) measurement with GROND instrument at the 2.2 m MPI/ESO telescope in the z band. The coloured hexagonal markers represent our data within the z-band wavelength range. The colours of the hexagonal points correspond to those in Fig. 8.

is likely causing the systematic relative flux variations seen in the 8835 Å observations (Fig. 11). Shown in Fig. 7 (fifth panel from the top) is the observed wavelength drifted towards shorter wavelengths during the night, with the OH line (red line) causing an increase in the relative flux. This is clearly seen in the raw transit light curve shown in Fig. 11 (middle green light curve on the right).

With the sky rings subtracted before performing aperture photometry, only very small sky-ring residuals are left in the images. It was of interest to investigate if other systematics were introduced by the wavelength drift sampling different parts of the spectrum of GJ 1214 or the spectra of one of the reference stars. Having previously conducted spectroscopic observations of GJ 1214 with the GTC telescope using the R500R grism and a 10 arcsec slit on

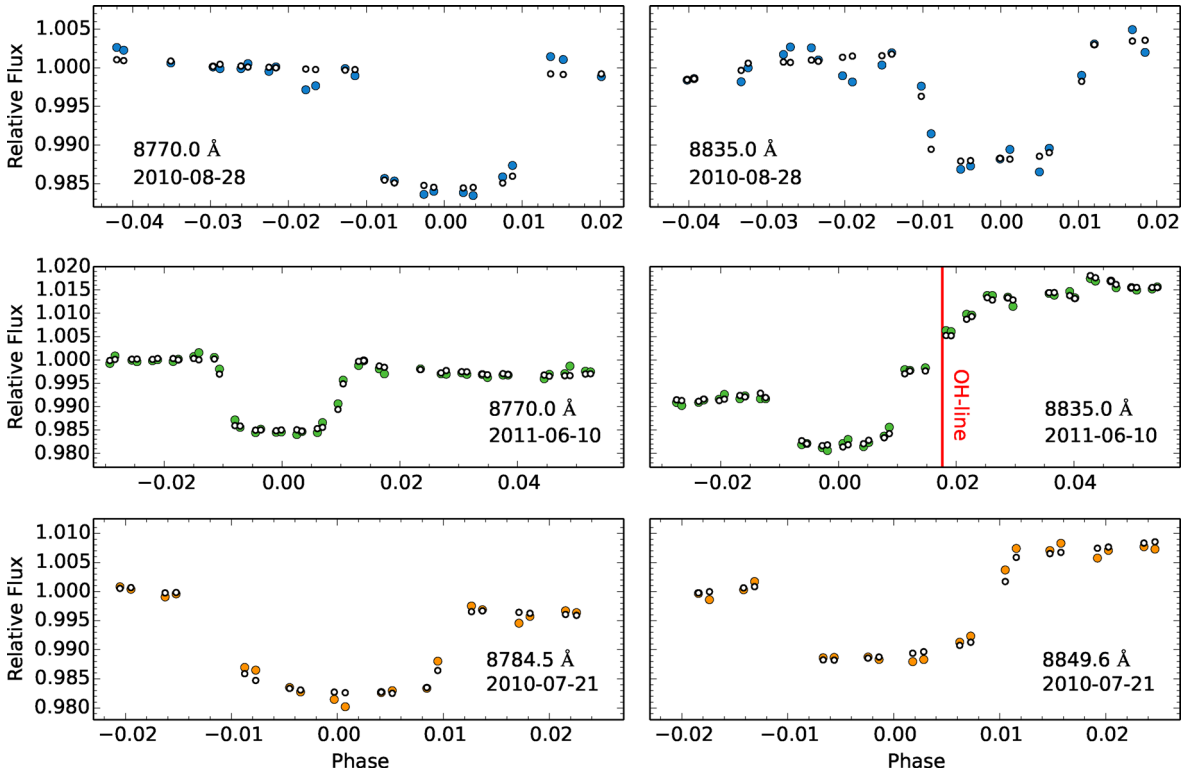

Figure 11. Shown are the raw (non-detrended) transit light curves at the off-methane target wavelengths 8770 Å (two transits) and 8784.5 Å (on the left) and the methane-probing target wavelengths 8835.0 Å (two transits) and 8849.6 Å (on the right). The hollow white points represent the best-fitting model. The red vertical line shows the phase during which the 8835 Å 2011 June 10 transit shows a wavelength drift across a strong OH-emission line doublet near 8829.5 Å (see Section 5.2).

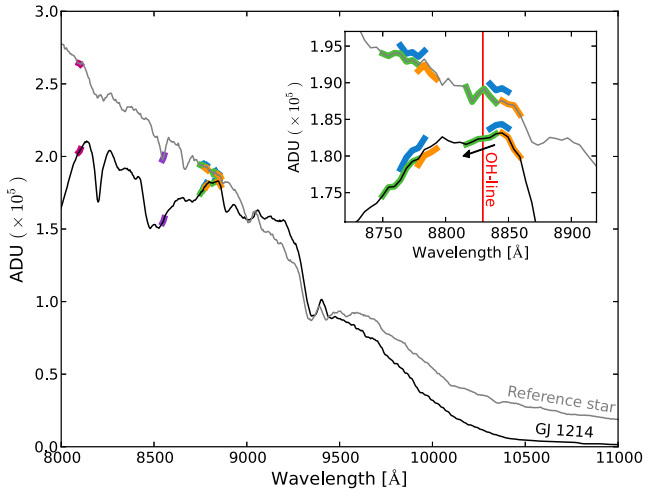

Figure 12. The spectrum of GJ1214 (black) and one of the reference stars with coordinates $17^h15^m19^s.42$ $04°56'32''.6$ (grey). The colours indicate the wavelength probed by each filer (including drifts). The reference spectrum has been multiplied by a factor of 9.2 to allow for a comparison in the sub-window. The OH doublet at the vacuum measured wavelengths 8829.514 and 8829.525 Å is shown in red. Only the 8835 Å observations on 2011 June 10 cross this line completely with the black arrow indicating the direction of the wavelength drift.

2012 July 25, we compared the wavelength drifts with the spectra of GJ1214 and one of the reference stars used. The two spectra which have a resolution of about $R \sim 250$ are shown in Fig. 12 with a rescaled view of the methane-probing region shown in the sub-window located towards the upper-right corner of the plot. Due to the nature of the long slit, only one other reference star could be fitted onto the slit. Since no major absorption lines were crossed, it is unlikely that the systematic wavelength trends are caused by different parts of the spectrum of GJ 1214 or the reference star being sampled.

5.3 Probing the methane feature

Here, we compare our five observed transits of GJ 1214b with theoretical models presented in Morley et al. (2013) to investigate the nature of GJ 1214b's atmosphere, in particular, to look for extra absorption due to methane (see Figs 8 and 9). Using tuneable narrow-band filters, we are able to probe the planets' atmosphere at a higher spectral resolution (R 600–750) than would otherwise be possible using standard photometric filters.

The possibility of a methane feature is explored by comparing the difference in radius ratios between the on-methane, off-methane observations each done on the same night. For the observations done on 2010 July 21, the differences in radius ratios were found to be $\Delta R = -0.0013 \pm 0.0031$, for 2010 August 28, $\Delta R = -0.0029 \pm 0.0041$, and for 2011 June 10, $\Delta R = 0.0004 \pm 0.0023$. The weighted average of the difference in radii from all three nights is calculated to be $\Delta\overline{R} = -0.0007 \pm 0.0017$, which in terms of scaleheights (H) is expressed as $\Delta\overline{R} \simeq -0.5 \pm 1.2H$, using $H/R_s = 0.0014$ and assuming a hydrogen-dominated atmosphere. We therefore detect no increase across a possible methane feature. This is also evident when comparing the transit depth differences between the light curves obtained on the same night (Fig. 13). A close-up of the probed methane

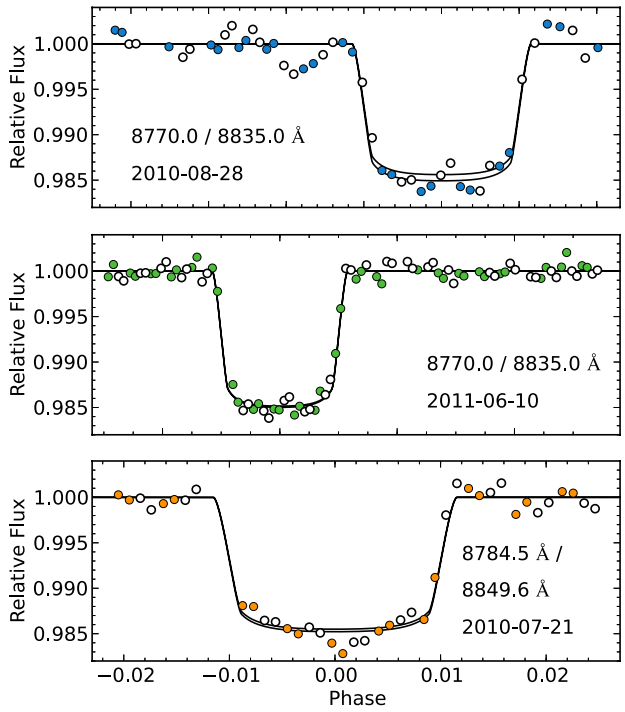

Figure 13. The GTC OSIRIS narrow-band light curves with the light curves obtained on the same night overplotted with their best-fitting models to enable direct comparison of the transit depth differences. The white points indicate the longer wavelength within each sequence.

region together with the weighted average of the on- and off-methane planet-to-star radius ratios is shown in Fig. 9.

5.4 Atmosphere models

We compare our observations across the methane feature to nine different atmosphere models, which include a 100 per cent water atmosphere model, four cloud-free models and four cloudy models from the model suites of Morley et al. (2013). Each of the cloudy and cloud-free models consists of solar (1×) and supersolar metallicities (50×) and a variety of *T*–*P* profiles. We find that our water and equilibrium cloud models (KCl and ZnS) fit the data well due to a large area of parameter space being allowed and are therefore not able to rule out any of the water or cloudy models. We show the worst-fitting cloudy model, a 50× solar composition atmosphere with a low sedimentation efficiency of $f_{\rm sed} = 0.1$ and an efficient heat distribution in Fig. 8. We are able to rule out all the cloud-free atmosphere models at the $>2.7\sigma$ level and show the best-fitting cloud-free models together with the worst-fitting cloudy model in Fig. 8.

A muted methane feature would require the presence of optically thicker clouds or a large mean molecular weight atmosphere which would be hard to detect, such as a water-dominated atmosphere. For a cloudy H-rich model to obscure the transmission spectrum, the clouds have to be optically thick high in the atmosphere where transmission spectroscopy probes ($\sim 10^{-3}$ bar). An inefficient heat redistribution would causes the *P*–*T* profile to be warmer, which would cause the profile to cross the condensation curve higher in the atmosphere. In addition, a low sedimentation efficiency would create a more vertically extended cloud. We note that photochemical models which include the formation of naturally forming photochemical hazes high in the atmosphere can also mute the transmission spectrum of GJ 1214b.

Croll et al. (2011) noted that the increased transit depth measured in the $K_{\rm s}$ band could be due to an opacity source such as methane or water, requiring hazes in the atmosphere. These measurements could also be explained by the observed spectral features being more complicated than current models predict. With a detection sensitivity of the order of a scaleheight at high spectral resolution, we are capable of excluding the presence of a methane absorption band spanning multiple scaleheights, which higher resolution models might reveal in the future.

6 CONCLUSIONS

We present GTC OSIRIS narrow-band observations of five transits of GJ 1214b, three of which probe the presence of methane at two near simultaneously obtained wavelengths. We do not find any increase in radius ratios across the possible methane feature with a planet-to-star radius ratio, $\Delta\overline{R} = -0.0007 \pm 0.0017$, across the feature. This corresponds to an increase in scaleheight of $-0.5 \pm 1.2H$ assuming a hydrogen-dominated atmosphere. We are therefore not able to rule out any of our water- and cloud-based models. Cloud-free models generally provide poor fits to the data. Even the best-fitting cloud-free model assuming a 50× solar composition atmosphere with an efficient heat distribution can be rejected at the 2.7σ confidence level form our data alone. The results, which are compatible with previous results of a largely flat transmission spectrum, do not rule out the possibility of a high-altitude haze or a water-dominated atmosphere in the atmosphere of GJ 1214b, but do rule out methane features spanning multiple scaleheights. Observations around the methane absorption band are predominantly limited by low-cadence observations and sky emission lines in the Earth's atmosphere affecting the photometric quality, making the determination of the systematic noise challenging. With TFs capable of high-resolution measurements ($R \approx 600$–750), there is currently a need for high-resolution methane models below 1 μm.

ACKNOWLEDGEMENTS

We thank the entire GTC staff and in particular Antonio Cabrera Lavers and Robert C. Morehead for their help in conducting these observations. This work is based on observations made with the GTC, installed at the Spanish Observatorio del Roque de los Muchachos of the Instituto de Astrofísica de Canarias on the island of La Palma. The GTC is a joint initiative of Spain (led by the Instituto de Astrofísica de Canarias), the University of Florida and Mexico, including the Instituto de Astronomía de la Universidad Nacional Autónoma de México (IA-UNAM) and Instituto Nacional de Astrofísica, Optica y Electrónica (INAOE). PAW, DKS and ARP acknowledge support from the UK Science and Technology Facilities Council (STFC). FP is grateful for the STFC grant and Halliday fellowship (ST/F011083/1). KDC and RCM were supported by the National Science Foundation (NSF) Graduate Research Fellowships. GEB acknowledges support from STScI through grants HST-GO-12473.01-A. This work was also aided by the National Geographic Society's Young Explorers Grant, awarded to KDC. The authors would like to acknowledge the anonymous referee for their useful comments.

REFERENCES

Bean J. L., Miller-Ricci Kempton E., Homeier D., 2010, Nature, 468, 669
Bean J. L. et al., 2011, ApJ, 743, 92
Berta Z. K., Charbonneau D., Bean J., Irwin J., Burke C. J., Désert J.-M., Nutzman P., Falco E. E., 2011, ApJ, 736, 12
Berta Z. K. et al., 2012, ApJ, 747, 35
Carter J. A., Winn J. N., Holman M. J., Fabrycky D., Berta Z. K., Burke C. J., Nutzman P., 2011, ApJ, 730, 82
Cepa J., 1998, Ap&SS, 263, 369
Cepa J. et al., 2000, in Iye M., Moorwood A. F., eds, Proc. SPIE Conf. Ser. Vol. 4008, Optical and IR Telescope Instrumentation and Detectors. SPIE, Bellingham, p. 623
Cepa J. et al., 2003, in Iye M., Moorwood A. F. M., eds, Proc. SPIE Conf. Ser. Vol. 4841, Instrument Design and Performance for Optical/Infrared Ground-based Telescopes. SPIE, Bellingham, p. 1739
Charbonneau D. et al., 2009, Nature, 462, 891
Collier Cameron A. et al., 2007, MNRAS, 380, 1230
Colón K. D., Gaidos E., 2013, ApJ, 776, 49
Colón K. D., Ford E. B., Lee B., Mahadevan S., Blake C. H., 2010, MNRAS, 408, 1494
Croll B., Albert L., Jayawardhana R., Miller-Ricci Kempton E., Fortney J. J., Murray N., Neilson H., 2011, ApJ, 736, 78
Crossfield I. J. M., Barman T., Hansen B. M. S., 2011, ApJ, 736, 132
de Mooij E. J. W. et al., 2012, A&A, 538, A46
Désert J.-M. et al., 2011a, A&A, 526, A12
Désert J.-M. et al., 2011b, ApJ, 731, L40
Fraine J. D. et al., 2013, ApJ, 765, 127
Gregory P. C., 2005, Bayesian Logical Data Analysis for the Physical Sciences: A Comparative Approach with 'Mathematica' Support. Cambridge Univ. Press, Cambridge
Hanuschik R. W., 2003, A&A, 407, 1157
Karkoschka E., 1994, Icarus, 111, 174
Kundurthy P., Agol E., Becker A. C., Barnes R., Williams B., Mukadam A., 2011, ApJ, 731, 123
Mandel K., Agol E., 2002, ApJ, 580, L171
Miller-Ricci E., Fortney J. J., 2010, ApJ, 716, L74
Morley C. V., Fortney J. J., Kempton E. M.-R., Marley M. S., Visscher C., Zahnle K., 2013, ApJ, 775, 33
Murgas F., Pallé E., Cabrera-Lavers A., Colón K. D., Martín E. L., Parviainen H., 2012, A&A, 544, A41
Narita N., Nagayama T., Suenaga T., Fukui A., Ikoma M., Nakajima Y., Nishiyama S., Tamura M., 2013a, PASJ, 65, 27
Narita N. et al., 2013b, ApJ, 773, 144
Nutzman P., Charbonneau D., 2008, PASP, 120, 317
Pont F., Zucker S., Queloz D., 2006, MNRAS, 373, 231
Pont F. et al., 2009, A&A, 502, 695
Rogers L. A., Seager S., 2010, ApJ, 716, 1208
Rousselot P., Lidman C., Cuby J.-G., Moreels G., Monnet G., 2000, A&A, 354, 1134
Sada P. V. et al., 2010, ApJ, 720, L215
Sing D. K., 2010, A&A, 510, A21
Sing D. et al., 2011, A&A, 527, A73
Teske J. K., Turner J. D., Mueller M., Griffith C. A., 2013, MNRAS, 431, 1669

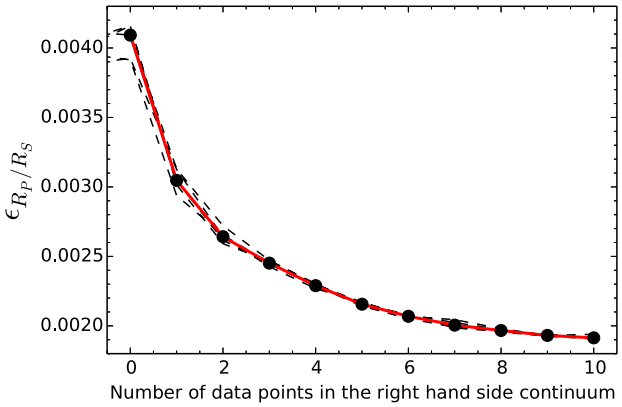

Figure A1. The uncertainties on the radius ratios as a function of the number of points in the right-hand continuum. The results from the five light curves are shown as dashed lines with their median value represented as a red solid line. The data consist of the 2010 August 28 8770 Å transit data with additional synthetic data points added to the right-hand continuum. As the number of data points in the right-hand-side continuum decrease, the uncertainty on the radius ratio given by the MCMC method increases following a power law.

APPENDIX A: SHORT BASELINES AND THE RADIUS RATIO UNCERTAINTY

With only a few data points present in the continuum of some of the transits, it was of interest to explore the effects of a short baseline on the uncertainty of the radius ratio as calculated using the MCMC method. To assess the relationship, we generated five light curves each consisting of the 2010 August 28 8770 Å transit data with additional synthetic data points added to the right-hand continuum. For each of the five light curves, a series of MCMC chains, each consisting of 500 000 steps (trimming away the first 50 000 points), were calculated iteratively removing one point from the right-hand continuum before calculating a new chain. This process was repeated for the five light curves with the resulting radius ratio uncertainties subsequently median combined. As shown in Fig. A1, as points are removed from the continuum, the radius ratio uncertainties as given by the MCMC method increase following a power law. The relationship is further verified by our observations when comparing the derived uncertainties on the radius ratio between the 2010-08-28 and the 2011-06-10 transits, which were done at the same wavelengths and show a consistent decrease in uncertainties with the addition of more points in the post-egress continuum.

This paper has been typeset from a TEX/LATEX file prepared by the author.